Monthly Notices
of the
ROYAL ASTRONOMICAL SOCIETY

MNRAS **477,** 2004–2019 (2018)
Advance Access publication 2018 March 17

doi:10.1093/mnras/sty719

The *Hubble Space Telescope* UV Legacy Survey of Galactic globular clusters – XIV. Multiple stellar populations within M 15 and their radial distribution⋆

D. Nardiello,[1,2†] A. P. Milone,[1] G. Piotto,[1,2] J. Anderson,[3] L. R. Bedin,[2] A. Bellini,[3] S. Cassisi,[4] M. Libralato[3] and A. F. Marino[5]

[1]*Dipartimento di Fisica e Astronomia 'Galileo Galilei', Università di Padova, Vicolo dell'Osservatorio 3, I-35122, Padova, Italy*
[2]*Istituto Nazionale di Astrofisica - Osservatorio Astronomico di Padova, Vicolo dell'Osservatorio 5, I-35122, Padova, Italy*
[3]*Space Telescope Science Institute, 3800 San Martin Drive, Baltimore, MD 21218, USA*
[4]*Osservatorio Astronomico d'Abruzzo, Via M. Maggini sn., I-64100 Teramo, Italy*
[5]*Research School of Astronomy and Astrophysics, The Australian National University, Cotter Road, Weston, ACT, 2611, Australia*

Accepted 2018 March 14. Received 2018 March 13; in original form 2018 February 22

ABSTRACT

In the context of the *Hubble Space Telescope* UV Survey of Galactic globular clusters (GCs), we derived high-precision, multi-band photometry to investigate the multiple stellar populations in the massive and metal-poor GC M 15. By creating for red-giant branch (RGB) stars of the cluster a 'chromosome map', which is a pseudo two-colour diagram made with appropriate combination of *F275W*, *F336W*, *F438W*, and *F814W* magnitudes, we revealed colour spreads around two of the three already known stellar populations. These spreads cannot be produced by photometric errors alone and could hide the existence of (two) additional populations. This discovery increases the complexity of the multiple-population phenomenon in M 15. Our analysis shows that M 15 exhibits a faint sub-giant branch (SGB), which is also detected in colour–magnitude diagrams (CMDs) made with optical magnitudes only. This poorly populated SGB includes about 5 per cent of the total number of SGB stars and evolves into a red RGB in the $m_{\rm F336W}$ versus $m_{\rm F336W} - m_{\rm F814W}$ CMD, suggesting that M 15 belongs to the class of Type II GCs. We measured the relative number of stars in each population at various radial distances from the cluster centre, showing that all of these populations share the same radial distribution within statistic uncertainties. These new findings are discussed in the context of the formation and evolution scenarios of the multiple populations.

Key words: techniques: photometric – stars: Population II – globular clusters: individual: NGC 7078.

1 INTRODUCTION

In the last few years, several scenarios for the formation and evolution of multiple stellar populations (MPs) in globular clusters (GCs) have been suggested. Some authors claim that GCs host a primordial first stellar generation (1G), and a second generation of stars (2G) formed from matter ejected by polluters belonging to the 1G (e.g. Ventura et al. 2001; Decressin et al. 2007; D'Antona et al. 2016).

An alternative possibility is that GCs host only a single generation of stars, and the distinct populations of stars with different abundance of helium and light elements would be the product of stellar interactions in the unique dense environment of proto-GCs (e.g. de Mink et al. 2009; Bastian et al. 2013; Denissenkov & Hartwick 2014; see Renzini et al. 2015, hereafter Paper V, for a critical discussion).

The *Hubble Space Telescope (HST) UV Legacy Survey of Galactic GCs* (GO-13297, PI: G. Piotto; Piotto et al. 2015, hereafter Paper I) is a *HST* treasury project aimed at discriminating among these scenarios and constraining the formation and evolution of MPs in GCs. Specifically, we collected *F275W*, *F336W*, and *F438W* images of 57 GCs previously observed in *F606W* and *F814W* bands (GO-10775, PI: A. Sarajedini; see Sarajedini et al. 2007) to characterize for the first time MPs in a large sample of clusters. This data

⋆Based on observations with the NASA/ESA *Hubble Space Telescope*, obtained at the Space Telescope Science Institute, which is operated by AURA, Inc., under NASA contract NAS 5-26555.

† E-mail: domenico.nardiello@unipd.it

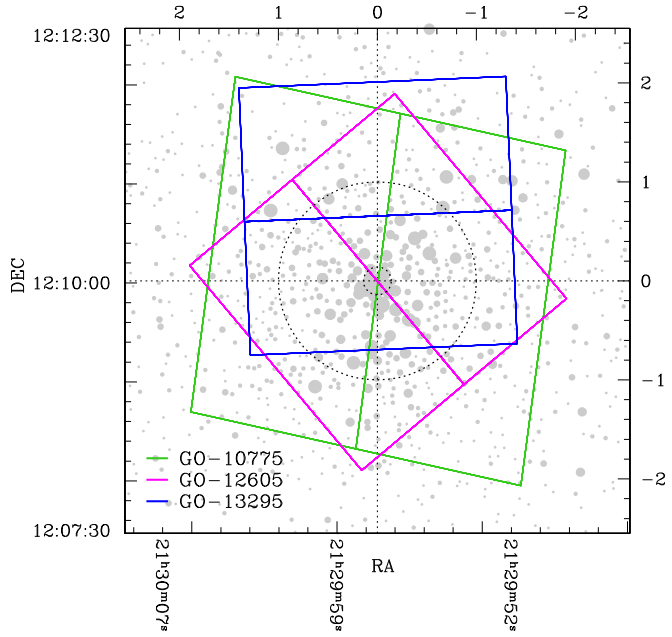

Figure 1. Footprint of the *HST* ACS and WFC3 observations used in this analysis. The inner circle is the core radius ($r_c = 0.14$ arcmin), and the outer circle is the half-light radius ($r_h = 1.0$ arcmin; Harris 1996, updated to 2010 December).

set is complemented by data previously collected from GO-12311 (PI: G. Piotto) and GO-12605 (PI: G. Piotto), which were pilot projects for GO-13297.

Results from this program have already provided a major breakthrough towards understanding the MP phenomenon. We have detected two or more populations in all the analysed GCs, thus suggesting that MPs are indeed ubiquitous in Galactic GCs (Paper I). The number of distinct populations, their chemical compositions, and the relative fractions of 2G and 1G stars dramatically change from one cluster to another, depending on the mass of the host GC. This fact suggests that cluster mass has played a major role to determine the MP phenomenon (Carretta et al. 2010; Milone et al. 2017, hereafter Paper IX).

Moreover, this unique data set allowed us to investigate the relative ages and the internal kinematics of the distinct populations (Bellini et al. 2015; Nardiello et al. 2015a).

Strong constraints on formation scenarios could be provided by the spatial distribution of MPs. Indeed, it has been suggested that 2G stars form in the innermost cluster region via cooling flow (e.g. D'Ercole et al. 2008, 2010). The fact that some clusters would still retain information on the initial distribution of 1G and 2G stars makes the study of their radial distribution a powerful tool to shed light on the MP phenomenon (Decressin, Baumgardt & Kroupa 2008; Vesperini et al. 2013).

In this context, NGC 7078 (M 15) is an intriguing case. The cluster M 15 is a massive ($\sim 5.6 \cdot 10^5\,M_\odot$; Marks & Kroupa 2010; Sollima & Baumgardt 2017), metal-poor Galactic GC ([Fe/H] ~ -2.37; Harris 1996, updated to 2010 December; Sobeck et al. 2011), characterized by many chemical peculiarities (see e.g. Lee 2000; Cohen, Briley & Stetson 2005; Carretta et al. 2009a; Pancino et al. 2010). It has been suggested that in the $\sim 2 \times 2$ arcmin^2 inner region of this cluster, 1G stars are more centrally concentrated than 2G stars (Larsen et al. 2015) in contrast with what is observed in other GCs (e.g. Sollima et al. 2007; Bellini et al. 2009, 2013; Milone et al. 2012c; Simioni et al. 2016, hereafter Paper X). At radial distances larger than ~ 2 arcmin, the radial trend is the opposite and 2G stars are more centrally concentrated than 1G stars (Lardo et al. 2011). Such an unusual, 'U-shaped' spatial distribution of 1G and 2G stars, if real, would be a major challenge for the scenarios of formation and evolution of MPs.

In this study, we exploit *HST* multi-band photometry to investigate the MPs within M 15 and derive their radial distribution. The paper is organized as follows. In Section 2 we describe the observations and the data reduction. We identify the multiple populations in Section 3, while in Section 4 we measure the relative fractions of stars in each population. The radial distribution of the distinct stellar populations is derived in Section 5. Summary and discussion are provided in Section 6.

2 OBSERVATIONS AND DATA REDUCTION

In this work we did not use the catalogues of Paper I, but we reduced all the useful *HST* data of M 15 available in the archive with new tools. These tools allowed us to obtain lower photometric errors for faint stars and produce artificial star catalogues, fundamental for our data analysis.

We reduced data collected with both cameras, the *HST* Wide Field Channel (WFC), which is part of the Advanced Camera for Surveys (ACS) and the UVIS imager of the Wide Field Camera 3 (WFC3). The observations cover the central region of the GC M 15. The total field of view is shown in Fig. 1, while Table 1 gives a detailed log of the observations. The analysis of the MPs hosted by M 15 is based on the data from GO-10775 (PI: A. Sarajedini), GO-12605 (PI: G. Piotto), and GO-13295 (PI: S. Larsen).

The M 15 catalogue belongs to the intermediate data-release of our project. The data reduction will be presented in a forthcoming paper (Nardiello et al., in preparation). In this analysis, we give a brief description of the major steps of the data reduction pipeline.

We worked on _FLC images, which are corrected for the charge-transfer inefficiency (Anderson & Bedin 2010). For each image we extracted a spatial- and time-varying array of point spread functions (PSFs) by perturbing library PSFs.[1] We used these PSF

[1] http://www.stsci.edu/~jayander/STDPSFs/

Table 1. Description of the archive *HST* images reduced in this analysis.

Program	Epoch	Filter	$N \times$ exp. time	Instrument	PI
10775	2006.33	*F606W*	15 s + 4 × 130 s	ACS/WFC	A. Sarajedini
10775	2006.33	*F814W*	15 s + 4 × 150 s	ACS/WFC	A. Sarajedini
12605	2011.80	*F275W*	2 × 615 s + 3× 700 s	WFC3/UVIS	G. Piotto
12605	2011.80	*F336W*	5 × 350 s	WFC3/UVIS	G. Piotto
12605	2011.80	*F438W*	5 × 65 s	WFC3/UVIS	G. Piotto
13295	2013.67	*F343N*	2 × 350 s	WFC3/UVIS	S.S. Larsen
13295	2013.67	*F555W*	2 × 10 s	WFC3/UVIS	S.S. Larsen

arrays to extract astro-photometric catalogues from the images. We corrected the positions of the stars for geometric distortion using the routines described by Anderson & King (2006, ACS/WFC), and by Bellini & Bedin (2009) and Bellini, Anderson & Bedin (2011, WFC3/UVIS). We adopted the catalogue associated with the deepest *F814W* exposure ($t_{\rm exp}$ = 150 s, j9l954fdq) as reference system for positions and we found the transformations between this master catalogue and all the other single-exposure catalogues, using six-parameter linear transformations. For each filter, the photometric zero-point of each filter in each individual catalogue is tailored to that of the deepest exposure. For each filter, we obtained a final catalogue containing the 3σ-clipped average stellar positions and fluxes in that filter ('first-pass' photometry, similar to that used in Paper I).

We extracted the 'second-pass' photometry using the FORTRAN routine KITCHEN_SYNC2 (KS2, J. Anderson, in preparation; Sabbi et al. 2016; Bellini et al. 2017). Using the images, the PSF arrays, and the transformations obtained during the 'first-pass' photometry, KS2 analysed all the images simultaneously to find and measure each source (after subtracting the neighbour stars) through eight different iterations. The KS2 software generated astrometric and photometric catalogues of stars using three different methods. A detailed description of the three methods is given in Bellini et al. (2017). In this analysis, we used only the method-1 measurements, which give the best results for the bright stars. The final catalogue of stars contains the positions (X, Y), the magnitudes in seven filters, and some quality parameters, such as the rms-based photometric errors, the quality-of-fit (QFIT), the number of images in which a star is found, and the number of good measurements used to measure the stellar flux. We calibrated the photometry into the Vega-mag system by comparing our PSF-based photometry against aperture photometry on _DRC images (which are normalized to an exposure time of 1 s; see Bellini et al. 2017 for details).

To characterize MPs along the sequences on the CMDs of M 15, we used only well-measured stars, selected as in Milone et al. (2012b), using different diagnostics such as photometric rms, QFIT, number of images in which the star is measured, etc. An example of selection of well-measured stars is shown in Fig. 2. Left panels of Fig. 2 show the selections based on the photometric rms (top panel) and on the QFIT (bottom panel) for the filter *F336W*. We performed similar selections for the other filters. The stars that passes the selection criteria in *F336W* and *F814W* filters are shown in the $m_{\rm F336W}$ versus $m_{\rm F336W} - m_{\rm F814W}$ CMD of the central panel of Fig. 2; right panel shows the stars that are rejected by at least in one filter.

We corrected the magnitudes for differential reddening (DR) using the procedure described in Milone et al. (2012c). Briefly, in a given CMD (where MPs are not evident), for each star in our catalogue, we selected the closest 50 cluster stars and measured their colour offset from the fiducial cluster sequence (along the reddening direction). The average and the standard deviation of the offsets were assumed to be the local estimate of the DR ($\delta E(B-V)$) and the error in this estimate is considered to be the correction error for the target star. To better constrain the variation of reddening in our field of view, we used the technique described in Milone (2015), based on the comparison of $\delta E(B-V)$ (i.e. the variation of the reddening from the average value of $E(B-V) = 0.1$) obtained from two different CMDs. The bottom left panel of Fig. 3 shows the procedure: we compared $\delta E(B-V)$ obtained from $m_{\rm F606W}$ versus $m_{\rm F336W} - m_{\rm F606W}$ and $m_{\rm F814W}$ versus $m_{\rm F438W} - m_{\rm F814W}$ CMDs, and then performed a least-squares fit to obtain the final value of $\delta E(B-V)$ (red line). The right panel illustrates the variation of $\delta E(B-V)$ over our field of view. The top panels show the $m_{\rm F336W}$ versus $m_{\rm F336W} - m_{\rm F814W}$ CMDs before (left panel) and after (right panel) the correction. The correction is more evident at the SGB level, because that is where the sequence is almost orthogonal to the reddening vector.

2.1 Artificial-star tests

In this analysis, we used artificial stars (ASs) for many different purposes: to determine the completeness level of the analysed stars, to estimate the impact of blends in the observed data, and to measure the fraction of stars belonging to each population hosted by M 15.

We produced ASs only for red-giant branch (RGB) stars, which are our main targets here. We covered a range of magnitude between $m_{\rm F814W} = 14.20$ and $m_{\rm F814W} = 17.30$. We generated 200 000 ASs with a flat luminosity function in *F814W* and with colours that lie along the RGB fiducial lines in the $m_{\rm F814W}$ versus $m_{\rm X} - m_{\rm F814W}$ CMDs, where X represents one of the available filters. The ASs have a Gaussian spatial distribution, centred on M 15 and with $\sigma = 70$ arcsec. The software added one AS at a time to each image with the appropriate position and flux, and then searched for the star and measured it using the same procedures adopted for real stars and giving the same outputs.

We studied the level of completeness at different magnitudes and radial distances from the centre of the cluster. We considered an artificial star to be recovered if the difference between the input and output positions is less than 0.5 pixel and if the difference between the input and output $m_{\rm F814W}$ magnitude is less than 0.75 mag. We found that the completeness for RGB stars is between 93 per cent (in the central region) and 99 per cent ($\gtrsim$ 1 arcmin from the centre of M 15).

3 THE CHROMOSOME MAPS AND THE MULTIPLE STELLAR POPULATIONS IN M 15

In Milone et al. (2015, hereafter Paper II) and Paper IX, we introduced a pseudo-two-colour diagram, or chromosome map (ChM), in order to separate stars with 1G- and 2G-type abundance patterns. We used this new tool to identify 1G and 2G stars in 57 GCs. In this work, we exploit the ChM to identify MPs along the RGB of

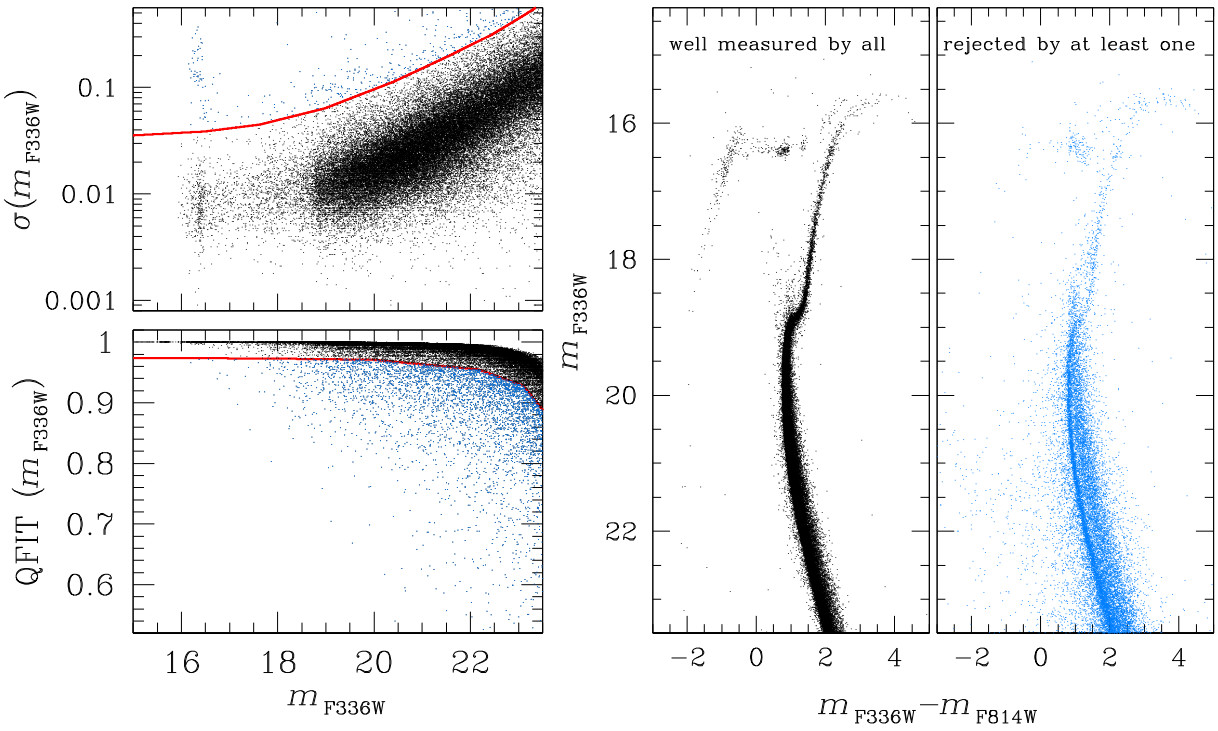

Figure 2. Selection of well-measured stars based on photometric errors (top-left panel) and QFIT (bottom-left panel), for the filter *F336W*: in black the stars that satisfy the selection criteria, in azure the rejected stars. Similar selections have been performed for the other filters. The CMD in the central panel shows the stars that passed the selections in the *F336W* and *F814W* filters; the right panel shows the CMD of the stars rejected by at least one of selection cuts.

M 15. We then calculated the number of stars in each population and studied their radial distribution.

In the following we describe the method we used to construct the ChMs by using the $m_{\rm F275W}$, $m_{\rm F336W}$, $m_{\rm F438W}$, and $m_{\rm F814W}$ filters. For a detailed description we refer to Paper IX.

We started by identifying isolated RGB stars using the $m_{\rm F814W}$ versus $m_{\rm F275W} - m_{\rm F814W}$ CMD (see Fig. 4); we excluded stars that are more distant than 0.17 mag in colour from the fiducial line of the RGB. The objects that we have rejected include evolved blue stragglers, photometric blends, and binaries with mass ratio close to one. The selected sample includes 1309 RGB stars, which are marked with green points in Fig. 4.

The procedure adopted to derive the $\Delta_{CF275W,\,F336W,\,F438W}$ versus $\Delta_{F275W,\,F814W}$ ChM is illustrated in Fig. 5. In panel (a_1) of Fig. 5 we highlight in black the RGB stars. We divided the RGB into a set of *F814W* magnitude bins (of width $\delta m = 0.4$ mag). We divided each bin in N sub-bins of width $\delta m/3$.

We calculated the 4th and the 96th percentiles of the colour distribution and the mean *F814W* magnitude in each interval $m^i_{\rm F814W} < m_{\rm F814W} < m^i_{\rm F814W} + \delta m$, with $i = 1, ..., N$. We used a three-point boxcar to smooth the 4th and the 96th points and then interpolated them with a spline for obtaining the blue (4th percentile) and red (96th percentile) lines shown in panels (b) and (c), respectively, for the cases of $m_{\rm F275W} - m_{\rm F814W}$ colour and $C_{\rm F275W,\,F336W,\,F43W} = (m_{\rm F275W} - m_{\rm F336W}) - (m_{\rm F336W} - m_{\rm F438W})$ pseudo-colour from Fig. 5.

For each colour C, we computed the observed RGB width $W_C^{\rm obs}$ as the difference between the colours of red and the blue lines at 2.0 *F814W* magnitudes above the MS turn-off ($m_{\rm F814W,\,TO} = 18.875 \pm 0.008$). We subtracted in quadrature the photometric and DR-correction errors to $W_C^{\rm obs}$, obtaining the intrinsic RGB width W.

For each star we computed the quantities:

$$\Delta_{\rm F275W,F814W} = W_X \frac{X - X_{\rm fiducialR}}{X_{\rm fiducialR} - X_{\rm fiducialB}} \quad (1)$$

and

$$\Delta_{CF275W,F336W,F438W} = W_Y \frac{Y_{\rm fiducialR} - Y}{Y_{\rm fiducialR} - Y_{\rm fiducialB}}, \quad (2)$$

where $X = (m_{\rm F275W} - m_{\rm F814W})$, $Y = C_{\rm F275W,\,F336W,\,F438W}$, 'fiducialR' and 'fiducialB' are the red and blue fiducial lines of panels (b) and (c) of Fig. 5. The verticalized RGBs are shown in the inset panels (b_1) and (c_1). Panel (d) shows the ChM $\Delta_{CF275W,\,F336W,\,F438W}$ versus $\Delta_{F275W,\,F814W}$ colours; the points in magenta are the distribution of the observational errors in the ChM, which are a combination of photometric and DR errors.

3.1 Multiple stellar populations along the RGB

The most prominent features of the ChM plotted in Fig. 5 are three groups of stars clustered around $\Delta_{CF275W,\,F336W,\,F438W} \sim 0.03$, 0.10, and 0.18. In panel (a) of Fig. 6 we have drawn by hand two dashed lines to select the corresponding main RGBs of M 15, which we call RGB-1, RGB-2, and RGB-3.

Noticeably, the triple RGB of M 15 was clearly visible in the $m_{\rm F336W}$ versus $C_{\rm F275W,\,F336W,\,F438W}$ pseudo CMD shown in Paper I (see their fig. 22) and was studied by Larsen et al. (2015) by using *F343N* and *F555W* WFC3/UVIS photometry. In the following, we demonstrate that the MP phenomenon in M 15 is even more complex than previously believed.

In Paper IX we discovered that the ChMs of all the analysed GCs, including M 15, host two distinct groups of 1G and 2G stars. The first generation of M 15 identified in Paper IX corresponds to the

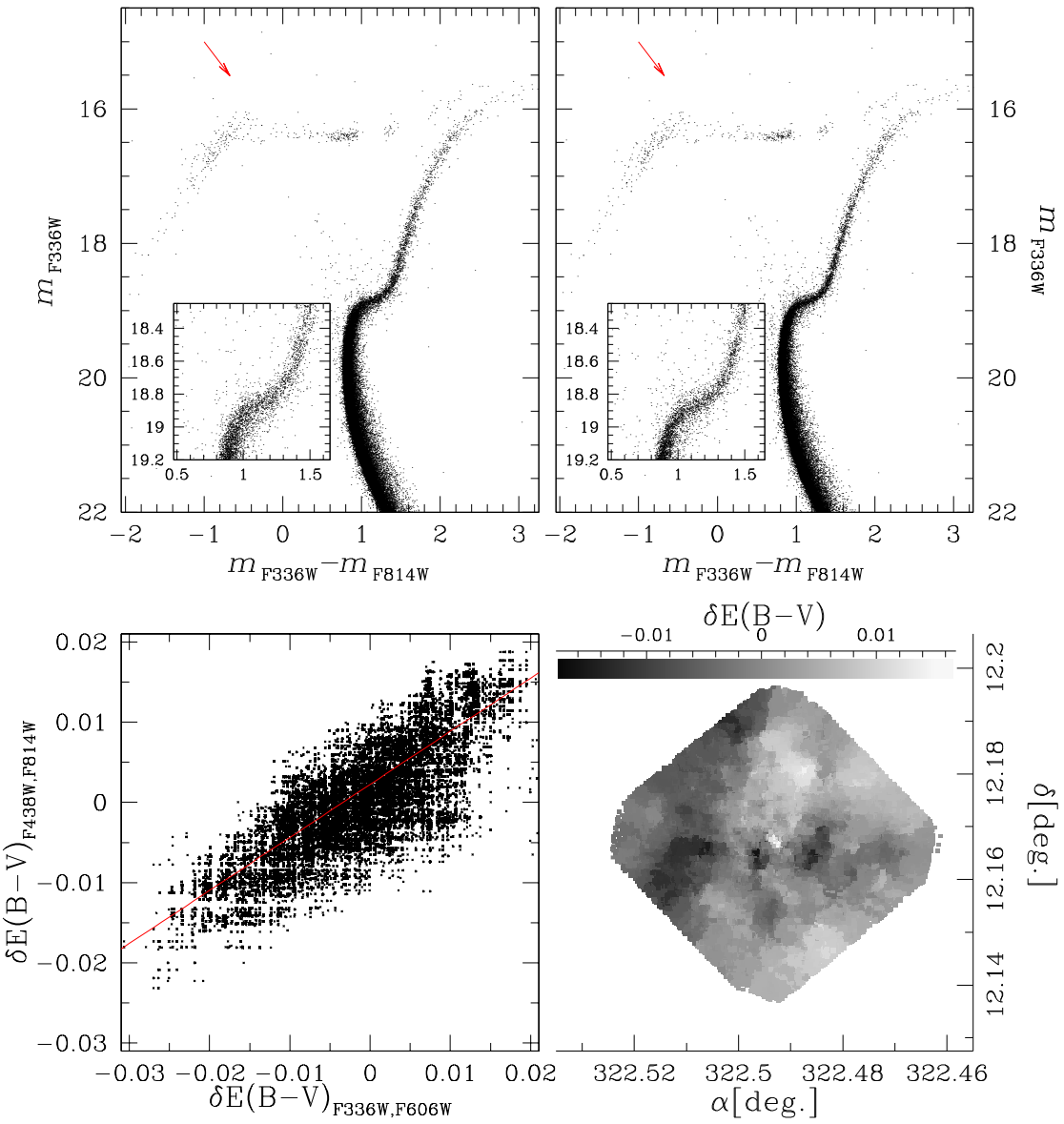

Figure 3. Top panels show the m_{F336W} versus $m_{F336W} - m_{F814W}$ CMDs before (left panel) and after (right panel) the differential reddening correction; the red arrow is the reddening vector. The insets show a zoom-in around the SGB region. Bottom left panel shows a comparison between the values of differential reddening inferred from m_{F606W} versus $m_{F336W} - m_{F606W}$ and m_{F814W} versus $m_{F438W} - m_{F814W}$ CMDs. The red line is obtained from a least-squares fit of the $\delta E(B-V)_{F336W,\,F606W}$ and $\delta E(B-V)_{F438W,\,F814W}$. Bottom right panel presents the map of the differential reddening.

RGB-1, while the second generation includes the sub-populations of RGB-2 and RGB-3 stars.

The ChM of M 15 reveals a complex morphology which is not adequately reproduced by only three simple stellar populations. As discussed in Paper IX, the $\Delta_{F275W,\,F814W}$ broadening of 1G stars is much larger than what we would expect from observational errors alone, thus indicating that the RGB-1 is not consistent with being a single, simple population. Moreover, we note a poorly populated group of RGB-3 stars spread around $\Delta_{F275W,\,F814W} \sim -0.1$ and $\Delta_{CF275W,\,F336W,\,F438W} \sim 0.25$.

To investigate the morphology of the RGB-1 we show in panel (b) of Fig. 6 a zoom of the m_{F336W} versus $m_{F336W} - m_{F814W}$ CMD around the RGB. In this CMD, as well, the colour spread of RGB-1 stars, which are represented with coloured circles, is much larger than what we expect from observational errors alone (∼0.015 mag for these bright stars), thus confirming that the RGB-1 is not composed by a simple homogeneous population. We drew by hand the black dashed line to separate the two sub-populations A and D of RGB-1 stars and coloured them red and cyan, respectively.

Similarly, in panel (c) of Fig. 6 we selected two sub-populations, C (blue circles) and E (orange circles), of RGB-3 stars. The location on the ChM of stars in the five populations of M 15 is provided in panel (d) of Fig. 6, where we indicate RGB-2 stars as population B. In the following we provide further evidence that the stellar groups A+D and C+E cannot be considered as simple stellar populations.

3.2 Populations D and E

In this section we show how the morphology of the ChM of M15 is better reproduced by adding the two stellar populations (POPs) D and E.

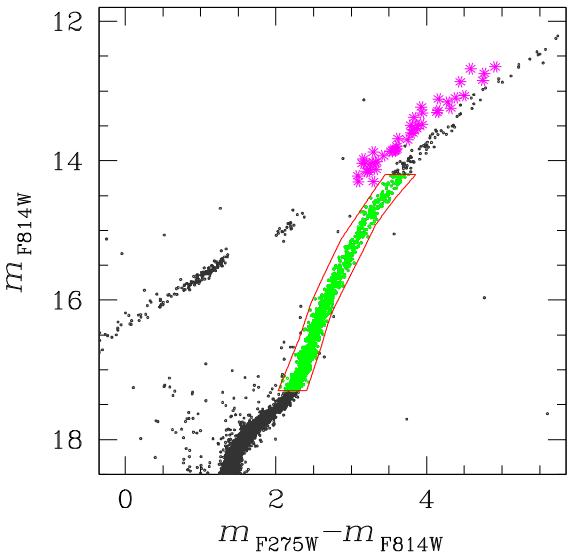

Figure 4. Selection of RGB (green) and AGB (magenta) stars based on the m_{F814W} versus $m_{F275W} - m_{F814W}$ CMD.

We first show that POP D and POP E stars are neither photometric blends nor stars with large observational errors. To do this, we adopted the procedure illustrated in Fig. 7, which is based on the comparison between the observed ChM of M 15 and the artificial-star simulated ChM of a single stellar population. To derive the latter, we added to the $\Delta_{F275W, F814W}$ and $\Delta_{CF275W, F336W, F438W}$ quantities derived from ASs the errors associated with the differential-reddening corrections. The observed and the simulated ChMs are plotted in panel (a) of Fig. 7.

In panels (b1) to (b3), we show that the $\Delta_{F275W, F814W}$ histogram distributions for populations A+D, B, and C+E are broader than the corresponding simulated distributions. A possible explanation is that each population A+D, B, and C+E host stars that are not chemically homogeneous. As an alternative, the difference between the dispersion of the simulated and observed $\Delta_{F275W, F814W}$ distributions could indicate that the magnitude errors inferred from ASs are simply lower limits on the real uncertainties on magnitude measurements.

To demonstrate that the groups of A+D and C+E stars are not simple populations, we first assumed that the magnitude errors inferred from ASs are underestimated. To compensate for this fact, we broadened the distribution of ASs by adding to each AS a

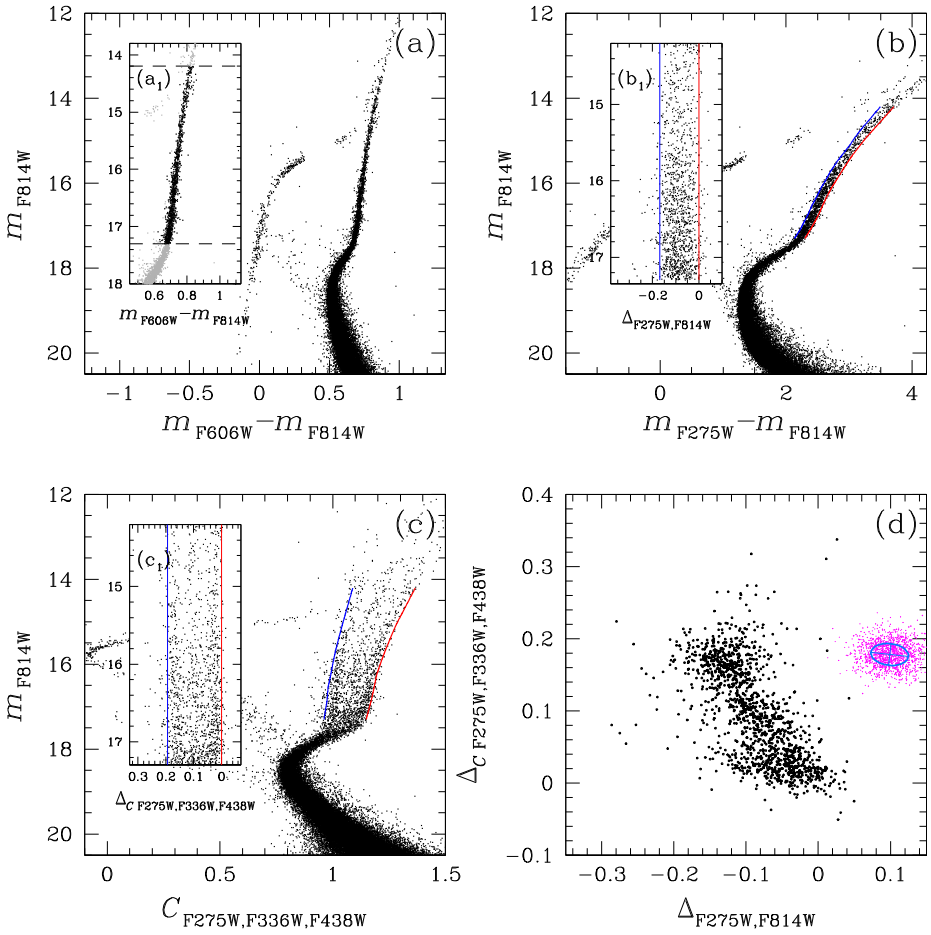

Figure 5. This figure illustrates the procedure adopted to derive the $\Delta_{CF275W, F336W, F438W}$ versus $\Delta_{F275W, F814W}$ ChM of RGB stars in M 15. Panel (a): the m_{F814W} versus $m_{F606W} - m_{F814W}$ CMD of M 15. The inset panel (a_1) shows a zoom-in on the RGB region: grey and black points represent all the well-measured stars and the selected RGB stars, respectively. Panels (b) and (c): the m_{F814W} versus $m_{F275W} - m_{F814W}$ and the m_{F814W} versus $C_{F275W, F336W, F438W}$ CMDs of M 15, respectively. The blue and red lines are the fiducials used to verticalize the RGB (inset panels (b_1) and (c_1)), and correspond to the 4th and 96th percentile of the RGB colour distribution. Panel (d): $\Delta_{CF275W, F336W, F438W}$ versus $\Delta_{F275W, F814W}$ ChM, obtained as explained in the text. The points in magenta are the distribution of the observational errors; the azure ellipse includes the 68.27 per cent of the points.

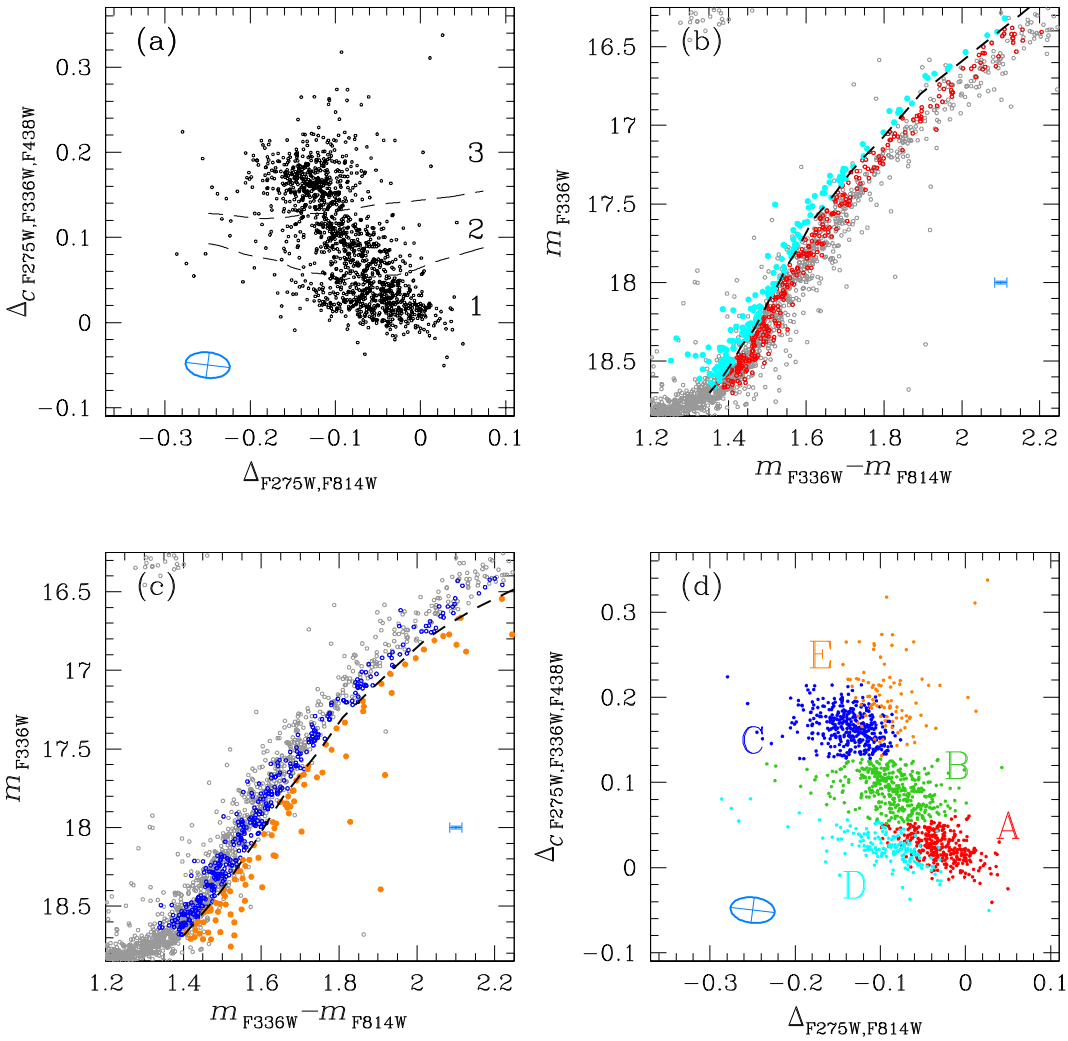

Figure 6. Procedure adopted to identify the different populations hosted by M 15. The dashed lines overimposed on the ChM shown in the panel (a) are used to identify the three groups of RGB-1, RGB-2, and RGB-3 stars. Panels (b) and (c) show the m_{F336W} versus $m_{F336W} - m_{F814W}$ CMD of RGB stars. The dashed lines plotted in the panels (b) and (c) are used to separate the two sub-populations A and D of the RGB-1 and the sub-populations C and E of the RGB-3, respectively. In panel (d) we use red, green, blue, cyan, and orange colours to represent stars in the populations A, B, C, D, and E, respectively, in the ChM. See text for details.

random noise in colour in such a way that the simulated histogram distribution matches the corresponding distribution of POP B stars. In doing this, we assume that POP B stars are chemically homogeneous, which might not be true. If the hypothesis is false, we are simply overestimating the photometric errors making the following conclusion on the reality on the A, D, C, and E populations even stronger.

Results are illustrated in panels (c1) to (c3) of Fig. 7 and show that the histograms of populations A+D and C+E (in black) exhibit a blue and a red tail, respectively. These tails are not present in the simulated histograms. Moreover, the AS dispersion is consistent with the observed dispersion of POP A and POP C only. We conclude that the stellar groups A–E selected in Fig. 6 are not artefacts but correspond to distinct stellar populations.

As an alternative method to demonstrate that the observed spreads in the ChM in the region corresponding to populations A and C are real, in Fig. 8 we analyse their position in the m_{F343N} versus $m_{F343N} - m_{F555W}$ CMD. The five sub-populations of M 15, including populations D and E, have been identified by using photometry in the *F275W*, *F336W*, *F438W*, and *F814W* bands (see Section 3.1) whereas the CMD of Fig. 8 comes from a data set, which is independent of that used in Section 3.1.

If the POP A+POP D are in fact a single population and the colour spread of the RGB made of POP A+POP D stars is due to photometric errors alone, then a star that is red (or blue) relative to the sequence in the diagrams of Section 3.1 should have the same probability of being either red or blue in the m_{F343N} versus $m_{F343N} - m_{F555W}$ CMD. By contrast, the fact that the two populations form two distinct sequences in the m_{F343N} versus $m_{F343N} - m_{F555W}$ CMD demonstrates that the colour spread of the POP A+POP D RGB is intrinsic and that the POP D stars have different photometric properties with respect to POP A (Anderson et al. 2009; Milone et al. 2010; Nardiello et al. 2015b). Similar arguments demonstrate that POP C and POP E are truly distinct sub-populations of M 15.

In this work we assume that POP A and POP D are two discrete populations, each one characterized by specific chemical properties. Because photometric errors do not allow us to totally split the colours of POP A and POP D in all colour–magnitude and two-colour diagrams, the hypothesis that the spread along the

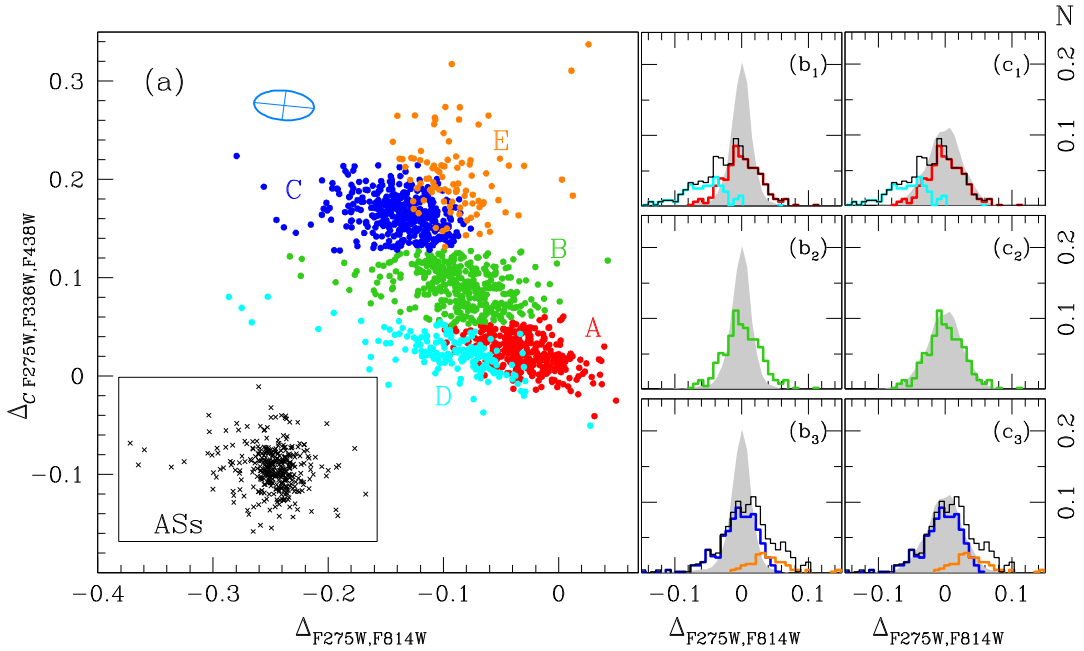

Figure 7. Left-panel: observed and simulated (in black) ChMs; colour codes for each observed population are as in Fig. 6. The azure ellipse is indicative of the observational errors. Right-panels: comparison between the $\Delta_{F275W,\,F814W}$ colour distributions of ASs (grey) and POP A, POP D, and POP A+POP D (in red, cyan, and black, respectively, panels (b1) and (c1)), POP B (green, panels (b2) and (c2)), and POP C, POP E, and POP C+E [in blue, orange, and black, respectively; panels (b3) and (c3)]. Panels (b) show the colour distribution of ASs as measured by the software KS2; in panels (c) we broadened the ASs colour distribution to take into account the underestimation of AS photometric errors. All the distributions are normalized to the total number of considered stars. See text for details.

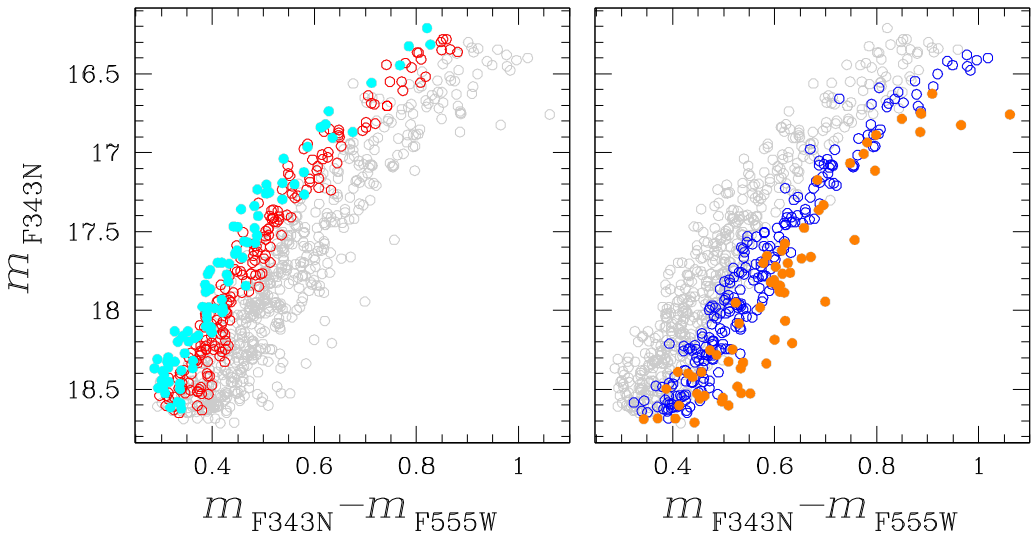

Figure 8. The m_{F343N} versus $m_{F343N} - m_{F555W}$ CMDs of RGB stars in M 15. Population A and D stars are coloured red and cyan. Blue and orange colours indicate populations C and E, respectively.

$\Delta_{F275W,\,F814W}$ colour in the ChM is due to a continuous (and not discrete) variation of chemical elements among the stars of the two populations cannot be excluded. Bearing in mind the above consideration, in the following analysis we will consider the scenario in which M15 hosts five distinct stellar populations.

Finally, we excluded that the colour distribution of POP A+POP D observed in the ChM is due to temperature effects. From the models we expect that stars located at the basis and at the top of the RGB sequence adopted to obtain the ChM have a difference in temperature of $\delta T_{\rm eff} \sim 1000$ K. A colour dependence by $\delta T_{\rm eff}$ would result in a dependence of the ChM on the luminosity, which is not observed.

3.3 The impact of binaries on the CMD

The POP D stars always form a sequence that is on average bluer than the POP A sequence; this fact might lead us to think that the POP D stars are binaries of POP A. We evaluated this hypothesis by performing a simulation of RGB POP A binary population using the procedure described in Milone et al. (2012b). We used ASs to

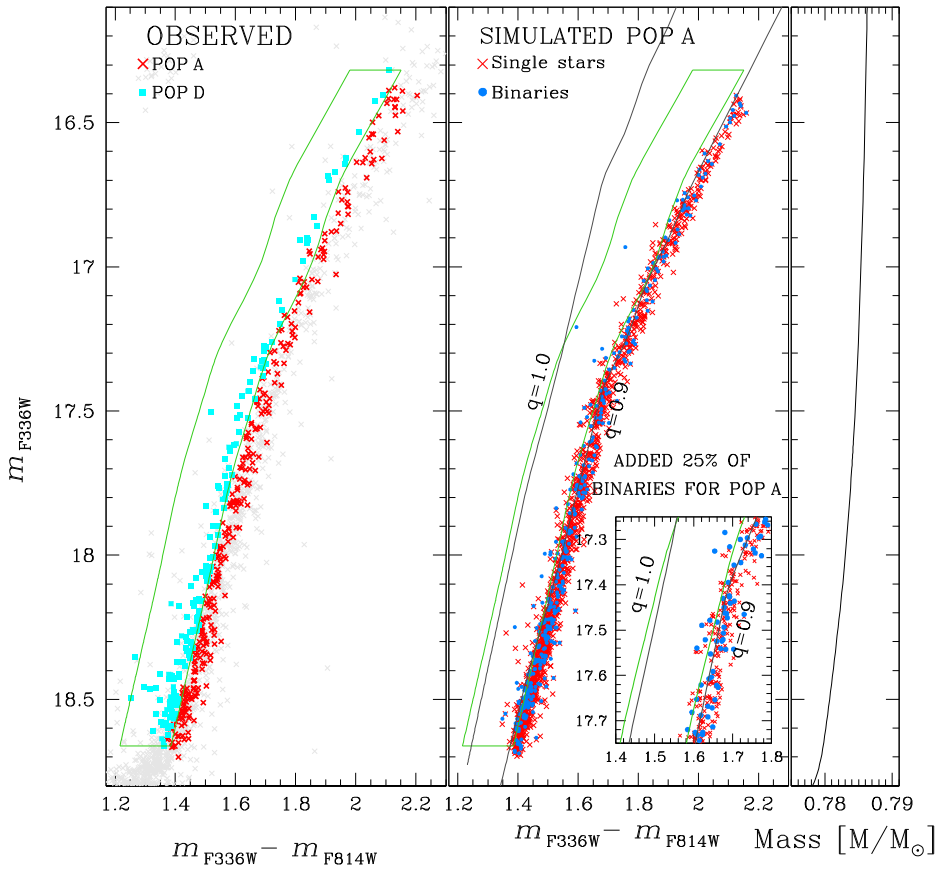

Figure 9. Procedure used to simulate the RGB binary population. Left panel: observed RGB sequences for POP A (red crosses) and POP D (cyan squares). The green region includes most of POP D stars. Middle panel: simulated RGB sequence for POP A (red crosses) and simulated POP A binary sequence (azure circles). Black lines are the loci of binary stars having mass ratios $q = 0.9$ and $q = 1.0$. In this simulation we added a fraction of stars equal to the 25 per cent of the total number of simulated RGB stars. Right panel: stellar mass as a function of the *F336W* magnitude.

simulate the $m_{\rm F336W}$ versus $m_{\rm F336W} - m_{\rm F814W}$ CMD of POP A. For each star in POP A we considered five ASs with *F814W* magnitudes within ± 0.10 and with radial distances within 25 pixels from the target star; in this way we took into account the contribution of possible blends to the final simulated CMD. As we did previously in Section 3.2, we also broadened the colour to simulate the spread of the sequence due to photometric errors. Fig. 9 shows the observed (left panel) and the simulated (middle panel) CMDs for POP A (red crosses). We derived the mass of the simulated RGB stars using the mass–luminosity relation of Dotter et al. (2007). We used an isochrone with age 13.25 Gyr, [Fe/H] $= -2.33$, [α/Fe] $= 0.20$ and primordial helium. The mass–luminosity relation is shown in the right panel of Fig. 9.

We chose to add to the simulated POP A a fraction of binary stars equal to 25 per cent of the total number of simulated POP A stars, with a flat mass (and luminosity) distribution. For each of these stars, having mass $\mathcal{M}_1$, we calculated the mass of the secondary star as $\mathcal{M}_2 = q \times \mathcal{M}_1$, with a mass ratio $0 < q \leq 1$. For the simulation we adopted a flat distribution for the mass ratios q. Using the mass–luminosity relation illustrated in right panel of Fig. 9, we obtained the luminosity of the secondary component. We added the fluxes of the two components in *F336W* and *F814W* bands, transformed them in magnitudes and replaced the original star in the CMD with this binary system. In Fig. 9 the binary stars are plotted in azure. When $q \lesssim 0.95$, the secondary star is a main-sequence star and the contribution of the secondary component to the total binary luminosity is negligible. For this reason, most of simulated binary stars (∼97 per cent) are indistinguishable from the simulated single-star RGB sequence. Only few binary stars fall inside the region (marked in green in the left and middle panels of Fig. 9) that contains most of POP D stars (cyan squares in the left panel of Fig. 9). In conclusion, assuming a flat mass distribution for the POP A binary components we expect that the bulk of RGB binaries is formed by a RGB + a MS star. Therefore, the probability that all POP D stars are binaries with mass ratio >0.95 is low,[2] we can also exclude the hypothesis that POP D represents a sequence of POP A binaries. With similar reasoning, POP D stars are also not binaries of POP B and POP C.

3.4 Multiple stellar populations along the SGB

Fig. 10 shows that the SGB of M 15 is not consistent with a single population. Specifically, the $m_{\rm F336W}$ versus $m_{\rm F336W} - m_{\rm F814W}$ CMD plotted in the upper panel shows a population of SGB stars that are spread below the bulk of the SGB stars. These stars, which have been selected in the $m_{\rm F336W}$ versus $m_{\rm F336W} - m_{\rm F814W}$ CMD (orange dots in top-panel of Fig. 10), define a stellar sequence that is fainter than the majority of SGB stars in all the CMDs, including those made

[2] Milone et al. (2012b) found that MS+MS binaries with $0.833 < q \leq 1.000$ are about 0.3 per cent of MS stars.

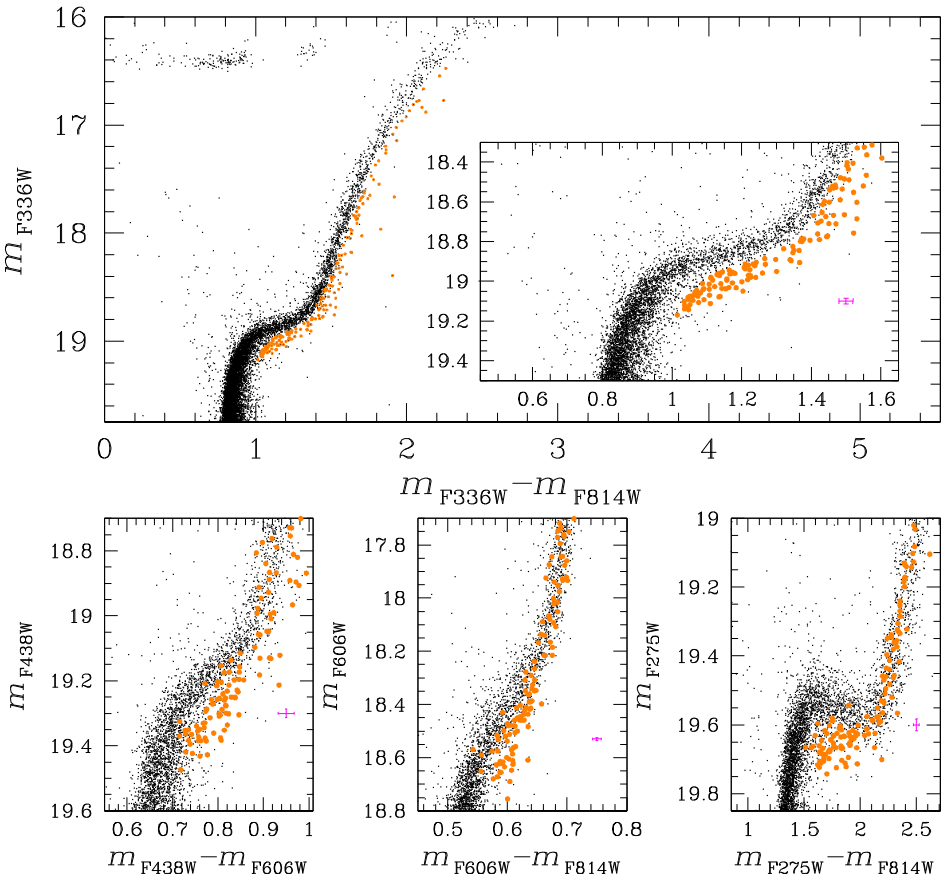

Figure 10. Top panel: m_{F336W} versus $m_{336W} - m_{814W}$ CMD of M 15, with the POP E coloured in orange. The inset shows a zoom-in around the SGB region. The faint SGB, possibly associated with POP E, is highlighted in orange. Bottom panels: m_{F438W} versus $m_{F438W} - m_{606W}$ (left), m_{F606W} versus $m_{F606W} - m_{814W}$ (middle), and m_{F275W} versus $m_{F275W} - m_{814W}$ (right) CMDs around the SGB region. The faint SGB stars selected in the top panel are coloured in orange in these CMDs as well. The magenta crosses show the photometric errors at the SGB level.

with only the optical bands. The faint SGB is clearly connected with the POP E RGB stars, which exhibit redder $m_{F336W} - m_{F814W}$ colours than the remaining RGB stars with the same luminosity.

Recently, Geller et al. (2017) have found a class of objects located in a CMD region redder than the MS and fainter than the SGB of many globular and open clusters. These sub-subgiant stars result to be evolved binary stars. The faint SGB we identify could be formed by sub-subgiant stars. However, we exclude this hypothesis for two reasons: (i) the faint SGB is connected to the POP E RGB; and (ii) the number of faint SGB stars (146) is much larger than the average number of sub-subgiant stars observed in some GCs (∼10 stars).

3.5 Multiple stellar populations along the asymptotic giant branch

Previous papers from our group have demonstrated that the m_{F814W} versus $C_{F275W, F336W, F438W}$ pseudo-CMD is also a powerful tool to identify multiple populations along the AGB (e.g. Papers II, III, V; Marino et al. 2017). The bottom-right panel of Fig. 11 reveals that the 45 AGB stars selected in Fig. 4 distribute along two distinct sequences of AGB_I (brown asterisks) and AGB_{II} stars (magenta triangles) in the m_{F814W} versus $C_{F275W, F336W, F438W}$ diagram. The selection of the two AGB groups has been performed in the $m_{F336W} - m_{F438W}$ versus $m_{F275W} - m_{F336W}$ diagram. The two groups of AGB_I and AGB_{II} contain (76 ± 17) per cent and (24 ± 11) per cent of AGB stars, respectively.

Fig. 11 provides a collection of m_{F814W} versus $m_X - m_{F814W}$ CMDs (X = *F275W, F336W, F343N, F438W, F555W*, and *F606W*), focused on the region around the AGB. The inset panels of the CMDs shown in Fig. 11 illustrate the average colour difference between AGB_I and AGB_{II} sequences. AGB_{II} sequence is, on average, bluer than AGB_I stars in all the CMDs, except in the m_{F814W} versus $m_{F555W} - m_{F814W}$ CMD, where the two groups share the same colour, and in the m_{F814W} versus $m_{F343N} - m_{F814W}$ CMD, where AGB_{II} stars are slightly redder than AGB_I stars. The maximum difference between AGB_I and AGB_{II} is ∼0.2 in the $m_{F275W} - m_{F814W}$ CMD.

These diagrams demonstrate that the AGB of M 15 hosts more than one stellar population. Spectroscopy is mandatory to connect multiple populations along the AGB and the RGB and to understand whether the RGB stars with extreme chemical composition ascend the AGB phase or avoid this evolutionary phase (Campbell et al. 2013, 2017; Cassisi et al. 2014; Lapenna et al. 2016; Marino et al. 2017).

4 POPULATION RATIOS

To determine the fraction of RGB stars in each of the five populations (POPs A–E), we extended to M 15 the technique introduced by our group in the investigation of NGC 2808 (Milone et al. 2012a; Paper X). At odds to what we have done in previous papers, which were based on the CMDs, here for the first time we exploit the ChM.

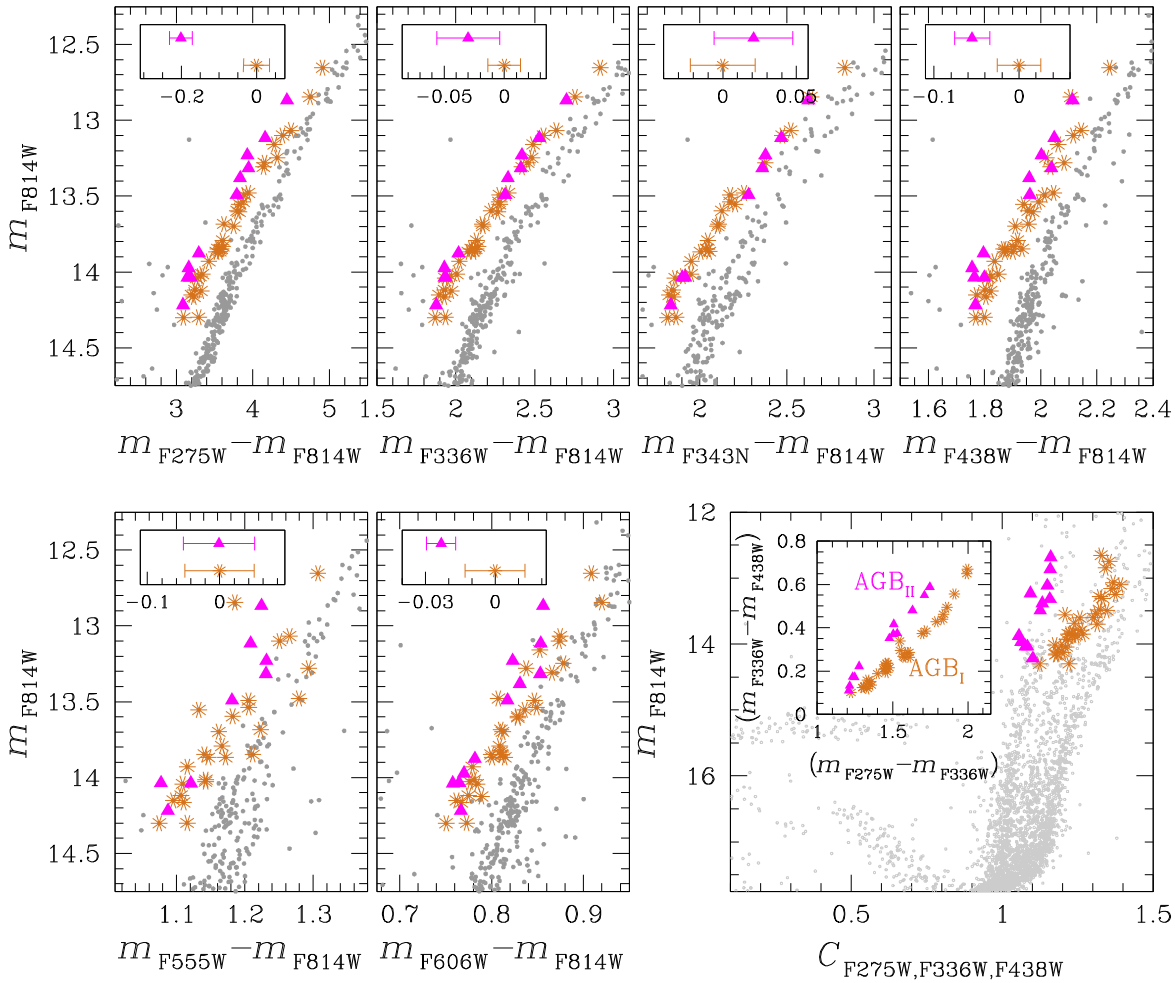

Figure 11. Analysis of AGB stars. Top-panels and first two bottom panels show the m_{F814W} versus $m_X - m_{F814W}$ CMDs, with X = *F275W*, *F336W*, *F343N*, *F438W*, *F555W*, and *F606W*; the inset panels show the average colour difference between AGB$_I$ and AGB$_{II}$ sequences. The right-hand bottom panel shows the m_{F814W} versus $C_{F275W,F336W,F438W}$ pseudo-CMD for all the stars (grey points) and for AGB stars (coloured points). Inset panel is the $m_{F336W} - m_{F438W}$ versus $m_{F275W} - m_{F336W}$ two-colour diagram of AGB stars. In all the diagrams, brown starred dots and magenta triangles represent the AGB$_I$ and AGB$_{II}$ stars, respectively.

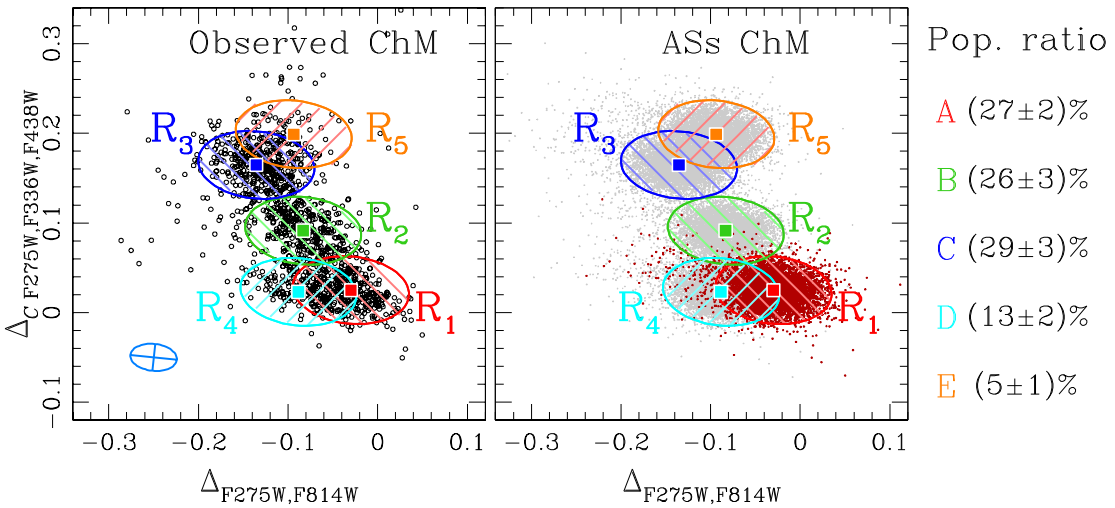

Figure 12. Procedure adopted to estimate the fraction of stars in each population. Left panel shows the observed $\Delta_{C\,F275W,\,F336W,\,F438W}$ versus $\Delta_{F275W,\,F814W}$ ChM (black empty circles). The azure ellipse is indicative of the dispersion of a single population (σ_{obs}). The regions R_i correspond to a size of 2.5 × σ_{obs}. Coloured squares correspond to the centre of the identified populations. Right panel shows the ASs $\Delta_{C\,F275W,\,F336W,\,F438W}$ versus $\Delta_{F275W,\,F814W}$ ChM. The regions R_i have the same size and are located in the same positions of the regions of the left panel.

We first defined five regions R_i, $i = 1, ..., 5$, in the ChM as shown in the left panel of Fig. 12. Each region is an ellipse centred on each sub-population of M 15 and is similar to the ellipse that best reproduces the distribution of the observational errors.

Since the stellar populations of M 15 are partially overlapped in the ChM, each region R_i would include stars from all the five sub-populations. Specifically, the number of stars within each region N_i can be expressed as:

$$N_i = N_{\rm A} f_i^{\rm A} + N_{\rm B} f_i^{\rm B} + N_{\rm C} f_i^{\rm C} + N_{\rm D} f_i^{\rm D} + N_{\rm E} f_i^{\rm E}$$
$$\text{with } i = 1, ..., 5, \quad (3)$$

where $N_{\rm A}$-$N_{\rm E}$ are the numbers of POP A-POP E stars in the ChM and $f_i^{\rm A-E}$ are the fractions of POP -POP E stars in the region R_i of the ChM.

To estimate the values of $f_i^{\rm A-E}$, we simulated the ChM of each stellar population of M 15 by using ASs and the same procedure described in the previous section. An example is provided in the right panel of Fig. 12 where we highlight the simulated ChM for POP A stars. The fractions of POP A stars in the five regions of the ChM, $f_i^{\rm A}$, are calculated as the ratio between the number of ASs within each region and the total number of simulated stars. We used the same method to determine $f_i^{\rm B-E}$.

To derive the number of stars in the ChM that belong to each population, $N_{\rm A}$-$N_{\rm E}$, we solved the system of five equations (3). We find that POP A, POP B, and POP C are the most populous stellar populations in M 15, making up (27 ± 2) per cent, (26 ± 3) per cent, and (29 ± 3) per cent of RGB stars, respectively. POP D contains (13 ± 2) per cent of RGB stars while POP E is formed by (5 ± 1) per cent of RGB stars.

Finally, we verified that the final result is not significantly affected either by the size of the regions R_i or by the exact location of their centres. In Fig. 12 we assumed that the lengths of both semi-axes of the ellipses are 2.5 times bigger than the corresponding dispersion expected for a single population ($\sigma_{\rm obs}$). We repeated the procedure by using ellipses with axes that are 2.0 and 3.0 bigger than $\sigma_{\rm obs}$ and find that the fractions of POP A–E stars are the same within 2 per cent. Similarly, we shifted the centres of each region by $\pm\frac{1}{2}$semimajor axis along $\Delta_{\rm F275W,\,F814W}$, and $\pm\frac{1}{2}$semiminor axis along $\Delta_{C\,\rm F275W,\,F336W,\,F438W}$ and find that the derived fractions of POP A–E stars remain unchanged within 2 per cent.

In Appendix we provide demonstrations of the reliability of the method that we used to derive the fraction of stars in each population.

5 THE RADIAL DISTRIBUTION OF MULTIPLE POPULATIONS

To derive the radial distribution of the stellar populations in M 15 we adopted two different techniques. We first calculated the median radial distance from the cluster centre of each population, $R_{\rm med,\,POP\,A\text{-}E}$, in close analogy with what has been done by Larsen et al. (2015). We expect that two populations with the same radial distribution would have the same value of $R_{\rm med}$, while different values of $R_{\rm med}$ would imply different radial distributions, with the more centrally concentrated population having also smaller values of $R_{\rm med}$.

Results are illustrated in the upper panel of Fig. 13 where we plot the $\Delta_{C\rm F275W,\,F336W,\,F438W}$ pseudo-colour of RGB stars as a function of the radial distance from the cluster centre.

We find: $R_{\rm med,\,POP\,A} = (37.6 \pm 1.4)$ arcsec (red line), $R_{\rm med,\,POP\,B} = (34.9 \pm 1.2)$ arcsec (green line), $R_{\rm med,\,POP\,C} = (38.1 \pm 1.3)$ arcsec (blue line), $R_{\rm med,\,POP\,D} = (33.5 \pm 1.8)$ arcsec (cyan line), $R_{\rm med,\,POP\,E} = (43.5 \pm 2.8)$ arcsec (orange line), with errors estimated via bootstrapping.

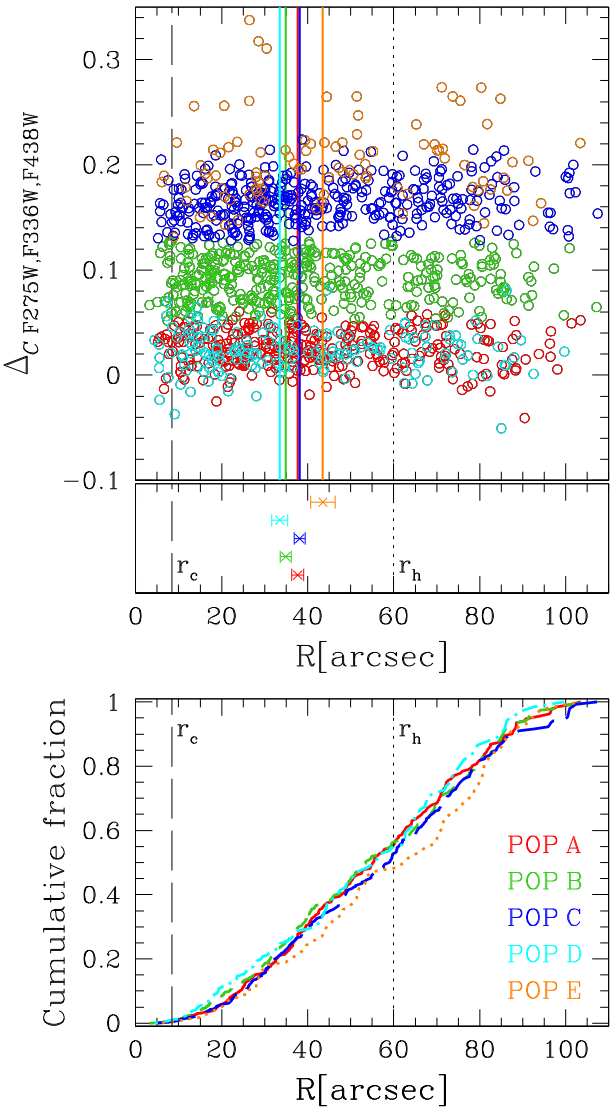

Figure 13. Top panel shows the pseudo-colour $\Delta_{C\rm F275W,\,F336W,\,F438W}$ as a function of the distance from the centre of M 15. The red, green, blue, cyan, and orange vertical lines are the median radial coordinates of POP A, POP B, POP C, POP D, and POP E, respectively. The median radial coordinates of the different populations are also reported in the middle panel, with the error-bars as shown. Bottom panel shows the cumulative radial distributions for each population. All populations share the same radial trend. Dashed and dotted vertical lines are the core (8.4 arcsec) and the half-light (60 arcsec) radii, as reported in Harris (1996, updated to 2010 December).

For completeness, we calculate the median radial distance for the sample of POP A+D, $R_{\rm med,POP\,A+D} = (36.7 \pm 1.2)$ arcsec, and of POP C+E stars, $R_{\rm med,POP\,C+E} = (38.7 \pm 1.3)$ arcsec.

All the measured values of $R_{\rm med,\,POP\,A\text{-}E}$ are consistent within 2.2 σ, thus demonstrating that none of the populations of M 15 is significantly more centrally concentrated than the others inside $\sim 2 \times r_{\rm h}$.

In the lower panel of Fig. 13, we compare the cumulative radial distributions of the five populations. The Kolmogorov–Smirnov test shows that all the populations are consistent with having the same radial distributions at the 95 per cent confidence level.

To compute the cumulative radial distribution and the median radial distance of POPs A-E, we adopted the identification of the stellar populations illustrated in Section 3.1 and in Fig. 6. Computing the radial distributions using this approach could give weak results, because of the overlapping of the different populations in the various CMDs and ChM.

As an alternative approach to deriving the radial distribution of MPs in M 15, we divided the field of view into five radial bins, each containing the same number of RGB stars (422). We applied the procedure described in Section 4 (that does not suffer from the problems due to the overlapping of the populations in the ChM) to the ChMs obtained with the stars in each radial bin; we derived the fraction of POP A–E stars in each radial interval; and we used them to analyse the radial distribution of each population.

The radial distributions of the five stellar populations are shown in panel (a) and zoomed in panels (c) of Fig. 14. In Table 2 we list the fractions of POP A–E stars in the five analysed radial bins.

As shown in Fig. 14 and Table 2, the distributions of all the populations are flat within the errors. The slopes of the best-fitting straight lines are: $(-5.9 \pm 4.0) \times 10^{-4}$ arcsec^{-1} (POP A); $(-1.2 \pm 3.1) \times 10^{-4}$ arcsec^{-1} (POP B); $(3.1 \pm 1.7) \times 10^{-4}$ arcsec^{-1} (POP C); $(1.4 \pm 4.8) \times 10^{-4}$ arcsec^{-1} (POP D); $(4.2 \pm 3.5) \times 10^{-4}$ arcsec^{-1} (POP E) and are consistent with zero within $\sim 2\,\sigma$.

Finally, in panel (b) of Fig. 14 we plot the radial distribution of the ratio between POP A+POP D and POP B+POP C+POP E stars (brown squares). These groups of stars correspond to the 1G and 2G as defined in Paper IX. We also show the ratio between the stars of POP A and of the remaining stellar populations as a function of the radial distance from the cluster centre (grey asterisks). The slopes of the straight lines that best match the brown and grey points are $(-11.0 \pm 7.7) \times 10^{-4}$ arcsec^{-1} and $(-13.5 \pm 9.6) \times 10^{-4}$ arcsec^{-1}, respectively. This demonstrates that in both cases the observations are consistent with a flat distribution within the errors.

6 SUMMARY AND CONCLUSIONS

As part of the *HST* UV survey of Galactic GCs (Paper I), we used multi-band *HST* photometry from GO-12605 and from the archive to investigate multiple populations in M 15 and to analyse their radial distribution.

Previous papers have shown that M 15 hosts three main groups of RGB stars (Paper I; Larsen et al. 2015). Our results increase the complexity of the multiple-population phenomenon in this GC. Indeed, by using the ChM, we provide evidence for spreads around POP A and POP C. These spreads are not compatible, within photometric errors, with the idea that such populations are composed by single stellar populations. An explanation of these spreads could be the presence of two additional populations. Specifically, the group of 1G stars, identified in Paper IX, includes two sub-populations, which we named A and D, while 2G stars include populations B, C, and E.

We derive the fraction of stars within each population with respect to the total number of RGB stars and find that the three dominant populations, A, B, and C, include (27 ± 2) per cent, (26 ± 3) per cent, and (29 ± 3) per cent of stars, respectively. POP D and POP E are less populated and host (13 ± 2) per cent and (5 ± 1) per cent of RGB stars, respectively.

M 15 exhibits a poorly populated SGB that is seen to be fainter than the majority of SGB stars in all the CMDs we were able to analyse, including those CMDs, like $m_{\rm F814W}$ versus $m_{\rm F606W} - m_{\rm F814W}$ and $m_{\rm F438W}$ versus $m_{\rm F438W} - m_{\rm F606W}$, that are constructed with optical filters only. Moreover, the faint SGB of M 15 seems to evolve into the RGB-E, which has redder $m_{\rm F336W} - m_{\rm F814W}$ colours than the bulk of RGB stars with the same luminosity.

In Paper IX we found that about 18 per cent of the 57 analysed clusters, hereafter Type II GCs, exhibit a number of distinctive features. These include a split SGB in optical CMDs with the faint SGB evolving into a red RGB in the $m_{\rm F336W}$ versus $m_{\rm F336W} - m_{\rm F814W}$ CMD. Moreover, red-RGB stars define a distinct locus in the ChM. Type II GCs have been widely investigated spectroscopically (e.g. Marino et al. 2015, see their table 10). In contrast with the majority of GCs, which are mono-metallic (e.g. Carretta et al. 2009b), the red-RGB stars and the faint SGB of these clusters are enhanced in metallicity, C+N+O, and in s-process elements with respect to the remaining cluster stars (e.g. Marino et al. 2009, 2011, 2012; Yong et al. 2009, 2014; Johnson et al. 2015, 2017). The photometric similarity between M 15 and the Type II GCs suggests that M 15 belongs to this class of clusters.

However, it is worth noting that M 15 shows no evidence for internal metallicity variations (Sneden 1999; Carretta et al. 2009b) but hosts two stellar groups with different abundances of Barium (Sneden 1999; Sobeck et al. 2011; Worley et al. 2013). Nevertheless, it is unlikely that the population of Ba-rich stars discovered by Sneden and collaborators, which includes about half of the analysed stars, corresponds to our POP E, which includes only ∼5 per cent of the total number of stars. Moreover, in contrast with other Type II GCs where the production of Barium is attributed to s-processes, the enhancement in Barium within M 15 has been associated with r-processes as indicated by the correlation between [Ba/Fe] and [Eu/Fe] (Sneden 1999). Spectroscopy of a large sample of stars, particularly including POP E stars, is mandatory to establish whether M 15 shares spectroscopic similarities with the other Type II GCs or not.

One important result of this paper concerns the radial distribution of MPs in M 15. The analysis of present-day radial distribution of 1G and 2G stars in GCs permits to discriminate between different formation scenarios of MPs in GCs.

Papers in the literature show that in some GCs, such as ω Cen, 47 Tuc, and NGC 2808, 2G stars are more centrally concentrated than the 1G stars (Sollima et al. 2007; Bellini et al. 2009; Lardo et al. 2011; Milone et al. 2012c; Bellini et al. 2018; Paper X). In other clusters, like NGC 6752 and M 5, 1G and 2G stars share the same distribution, indicating that the two populations are mixed due to dynamical evolution (e.g. Milone et al. 2013; Nardiello et al. 2015b; Lee 2017).

The possibility that 2G stars formed in the central regions of the proto-GCs has been recently challenged by Larsen et al. (2015). These authors have detected three stellar populations along the RGB of M 15 and found that the population with primordial chemical composition is the most centrally concentrated.

In this paper, we have demonstrated that the stellar populations hosted by this short-relaxation-time (half-mass relaxation time $t(r_{\rm h}) \sim 9.32$; Harris 1996, updated to 2010 December), post-core-collapse system share the same radial distribution, in contrast with previous conclusions. Moreover, we were able to verify that the group formed by POP A and POP D stars, which approximately corresponds to the stellar population with primordial chemical composition, has the same radial distribution as second-generation stars.

ACKNOWLEDGEMENTS

We thank the anonymous referee for the useful comments and suggestions. DN and GP acknowledge support by the Università degli Studi di Padova Progetto di Ateneo CPDA141214, 'Towards Understanding Complex Star Formation in Galactic Globular

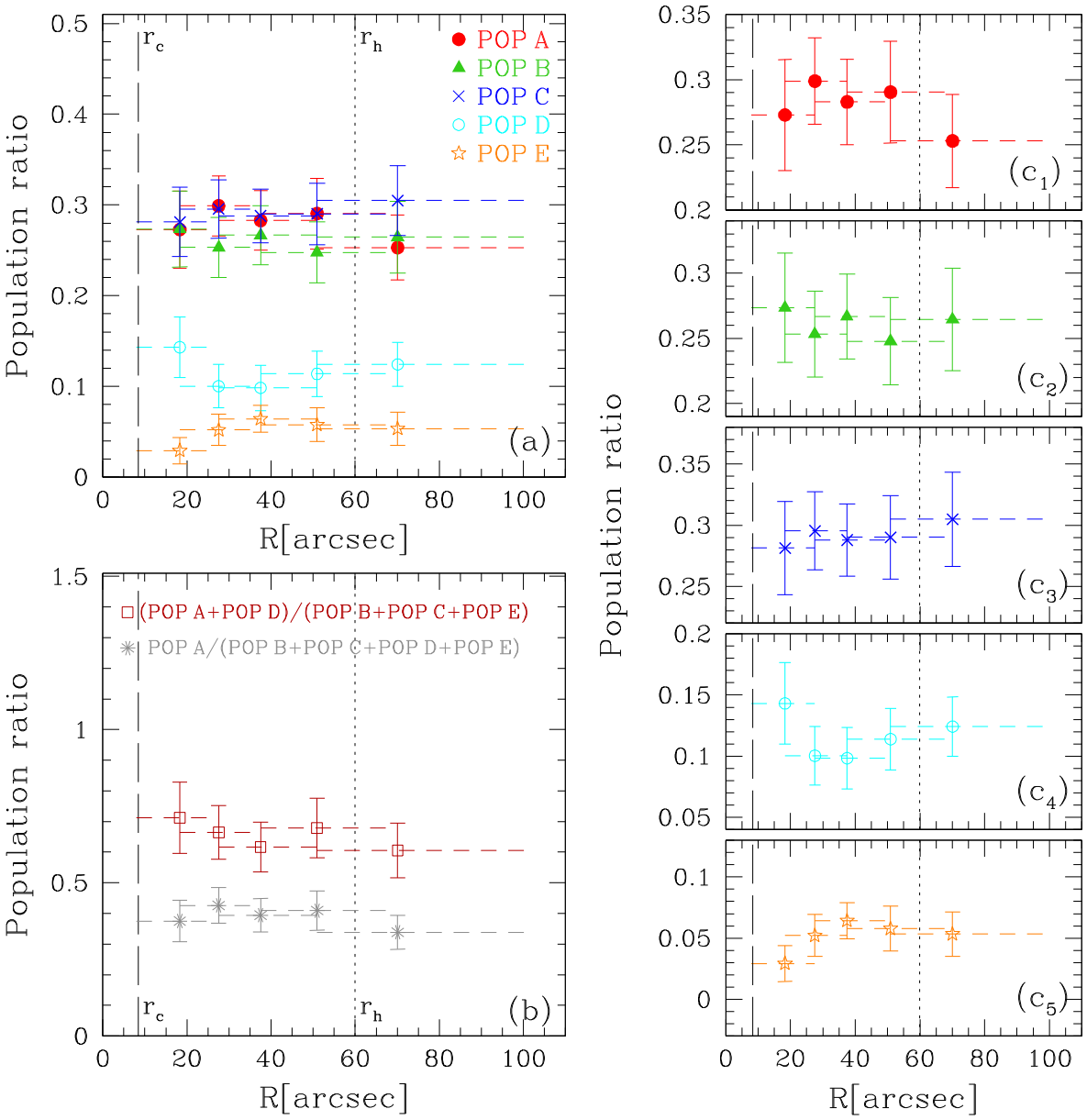

Figure 14. The radial distributions of the five stellar populations hosted by M 15 are shown in panel (a). Panel (b) shows the radial distribution of 1G/2G stars under two different hypotheses: (i) 1G is composed by only POP A stars (in grey); (ii) 1G is formed by POP A and POP D stars (in brown). Panels (c) are a zoom on the radial distribution of each single population. In all the panels, dashed and dotted vertical lines are the core and the half-light radii, as reported in Harris (1996, updated to 2010 December).

Table 2. Fraction of POP A, POP B, POP C, POP D, and POP E stars at different radial distances from M 15 centre.

R_{min} [arcsec]	R_{max} [arcsec]	R_{ave} [arcsec]	$f_{POP\,A}$	$f_{POP\,B}$	$f_{POP\,C}$	$f_{POP\,D}$	$f_{POP\,E}$
7.95	27.51	18.31	0.27 ± 0.04	0.27 ± 0.04	0.28 ± 0.04	0.15 ± 0.03	0.03 ± 0.01
18.31	37.46	27.55	0.30 ± 0.03	0.25 ± 0.03	0.30 ± 0.03	0.10 ± 0.02	0.05 ± 0.02
27.55	50.93	37.52	0.28 ± 0.03	0.27 ± 0.03	0.29 ± 0.03	0.10 ± 0.03	0.06 ± 0.02
37.52	70.08	50.95	0.29 ± 0.04	0.25 ± 0.03	0.29 ± 0.03	0.11 ± 0.02	0.06 ± 0.02
50.95	101.37	70.10	0.25 ± 0.04	0.27 ± 0.04	0.31 ± 0.04	0.12 ± 0.02	0.05 ± 0.02

Clusters'. GP and ML acknowledge support by PRIN-INAF2014, 'The Kaleidoscope of Stellar Populations in Galactic Globular Clusters with *Hubble Space Telescope*'. APM acknowledges support by the European Research Council through the ERC-StG 2016 project 716082 'GALFOR'.AFM has been supported by the Australian Research Council through Discovery Early Career Researcher Award DE160100851. JA acknowledges the support of STScI grant GO-13297.

REFERENCES

Anderson J., Bedin L. R., 2010, PASP, 122, 1035
Anderson J., King I. R., 2006, Technical report, PSFs, Photometry, and Astronomy for the ACS/WFC
Anderson J., Piotto G., King I. R., Bedin L. R., Guhathakurta P., 2009, ApJ, 697, L58
Bastian N., Lamers H. J. G. L. M., de Mink S. E., Longmore S. N., Goodwin S. P., Gieles M., 2013, MNRAS, 436, 2398
Bellini A., Bedin L. R., 2009, PASP, 121, 1419
Bellini A., Piotto G., Bedin L. R., King I. R., Anderson J., Milone A. P., Momany Y., 2009, A&A, 507, 1393
Bellini A., Anderson J., Bedin L. R., 2011, PASP, 123, 622
Bellini A. et al., 2013, ApJ, 765, 32
Bellini A. et al., 2015, ApJ, 810, L13
Bellini A., Anderson J., Bedin L. R., King I. R., van der Marel R. P., Piotto G., Cool A., 2017, ApJ, 842, 6
Bellini A. et al., 2018, ApJ, 853, 86
Campbell S. W. et al., 2013, Nature, 498, 198
Campbell S. W., MacLean B. T., D'Orazi V., Casagrande L., de Silva G. M., Yong D., Cottrell P. L., Lattanzio J. C., 2017, A&A, 605, A98
Carretta E. et al., 2009a, A&A, 505, 117
Carretta E., Bragaglia A., Gratton R., D'Orazi V., Lucatello S., 2009b, A&A, 508, 695
Carretta E., Bragaglia A., Gratton R. G., Recio-Blanco A., Lucatello S., D'Orazi V., Cassisi S., 2010, A&A, 516, A55
Cassisi S., Salaris M., Pietrinferni A., Vink J. S., Monelli M., 2014, A&A, 571, A81
Cohen J. G., Briley M. M., Stetson P. B., 2005, AJ, 130, 1177
D'Antona F., Vesperini E., D'Ercole A., Ventura P., Milone A. P., Marino A. F., Tailo M., 2016, MNRAS, 458, 2122
D'Ercole A., Vesperini E., D'Antona F., McMillan S. L. W., Recchi S., 2008, MNRAS, 391, 825
D'Ercole A., D'Antona F., Ventura P., Vesperini E., McMillan S. L. W., 2010, MNRAS, 407, 854
de Mink S. E., Pols O. R., Langer N., Izzard R. G., 2009, A&A, 507, L1
Decressin T., Meynet G., Charbonnel C., Prantzos N., Ekström S., 2007, A&A, 464, 1029
Decressin T., Baumgardt H., Kroupa P., 2008, Astron. Nachr., 329, 976
Denissenkov P. A., Hartwick F. D. A., 2014, MNRAS, 437, L21
Dotter A., Chaboyer B., Jevremović D., Baron E., Ferguson J. W., Sarajedini A., Anderson J., 2007, AJ, 134, 376
Geller A. M. et al., 2017, ApJ, 840, 66
Harris W. E., 1996, AJ, 112, 1487
Johnson C. I., Rich R. M., Pilachowski C. A., Caldwell N., Mateo M., Bailey III J. I., Crane J. D., 2015, AJ, 150, 63
Johnson C. I., Caldwell N., Rich R. M., Mateo M., Bailey III J. I., Clarkson W. I., Olszewski E. W., Walker M. G., 2017, ApJ, 836, 168
Lapenna E. et al., 2016, ApJ, 826, L1
Lardo C., Bellazzini M., Pancino E., Carretta E., Bragaglia A., Dalessandro E., 2011, A&A, 525, A114
Larsen S. S., Baumgardt H., Bastian N., Brodie J. P., Grundahl F., Strader J., 2015, ApJ, 804, 71
Lee S. G., 2000, J. Korean Astron. Soc., 33, 137
Lee J.-W., 2017, ApJ, 844, 77
Marino A. F., Milone A. P., Piotto G., Villanova S., Bedin L. R., Bellini A., Renzini A., 2009, A&A, 505, 1099
Marino A. F. et al., 2011, A&A, 532, A8
Marino A. F. et al., 2012, A&A, 541, A15
Marino A. F. et al., 2015, MNRAS, 450, 815
Marino A. F. et al., 2017, ApJ, 843, 66
Marks M., Kroupa P., 2010, MNRAS, 406, 2000
Milone A. P., 2015, MNRAS, 446, 1672
Milone A. P. et al., 2010, ApJ, 709, 1183
Milone A. P., Piotto G., Bedin L. R., Cassisi S., Anderson J., Marino A. F., Pietrinferni A., Aparicio A., 2012a, A&A, 537, A77
Milone A. P. et al., 2012b, A&A, 540, A16
Milone A. P. et al., 2012c, ApJ, 744, 58
Milone A. P. et al., 2013, ApJ, 767, 120
Milone A. P. et al., 2015, MNRAS, 447, 927 (Paper II)
Milone A. P. et al., 2017, MNRAS, 464, 3636 (Paper IX)
Nardiello D. et al., 2015a, MNRAS, 451, 312
Nardiello D., Milone A. P., Piotto G., Marino A. F., Bellini A., Cassisi S., 2015b, A&A, 573, A70
Pancino E., Rejkuba M., Zoccali M., Carrera R., 2010, A&A, 524, A44
Piotto et al., 2015, AJ, 149, 91 (Paper I)
Renzini A. et al., 2015, MNRAS, 454, 4197 (Paper V)
Sabbi E. et al., 2016, ApJS, 222, 11
Sarajedini A. et al., 2007, AJ, 133, 1658
Simioni M., Milone A. P., Bedin L. R., Aparicio A., Piotto G., Vesperini E., Hong J., 2016, MNRAS, 463, 449 (Paper X)
Sneden C., 1999, Ap&SS, 265, 145
Sobeck J. S. et al., 2011, AJ, 141, 175
Sollima A., Baumgardt H., 2017, MNRAS, 471, 3668
Sollima A., Ferraro F. R., Bellazzini M., Origlia L., Straniero O., Pancino E., 2007, ApJ, 654, 915
Ventura P., D'Antona F., Mazzitelli I., Gratton R., 2001, ApJ, 550, L65
Vesperini E., McMillan S. L. W., D'Antona F., D'Ercole A., 2013, MNRAS, 429, 1913
Worley C. C., Hill V., Sobeck J., Carretta E., 2013, A&A, 553, A47
Yong D., Grundahl F., D'Antona F., Karakas A. I., Lattanzio J. C., Norris J. E., 2009, ApJ, 695, L62
Yong D. et al., 2014, MNRAS, 441, 3396

APPENDIX: RELIABILITY OF THE MEASURED FRACTION OF MP STARS

To test the reliability of the method adopted in Section 4, we built 500 synthetic $\Delta_{CF275W,\,F336W,\,F438W}$ versus $\Delta_{F275W,\,F814W}$ ChMs with five different populations. Each synthetic population is obtained as follows. We first constructed the ChM of a single population using the ASs, as explained in Section 4. From this sample of stars we randomly extracted $N_{synth} + \Delta N_{synth}$ stars, where ΔN_{synth} is a random number between -50 and 50 and N_{synth} is a number different for each simulated population, in such a way that the final number of stars in the simulated ChM is similar to the number of stars in the observed ChM. In particular, we adopted $N_{synth} = (350, 350, 350, 150, 60)$ for POP (A,B,C,D,E), respectively. We centred each synthetic population in the centres of the observed population. Panel (a) of Fig. A1 shows a realization of the synthetic ChM. Panel (b) is the ASs ChM used to estimate the contamination of each population X in the region R_Y centred and containing the bulk of the population Y. We measured the fraction of stars that belong to each population using the technique illustrated in Section 4. The bottom panel shows the comparison between the fraction of stars measured from the synthetic ChM and the fraction of stars expected for each of the 500 realizations and for each of the simulated population. The error bars are obtained as explained in Section 4, and are a combination of Poissonian error, uncertainty on the centre and size of the adopted regions; inside the errors the measured fraction of stars reproduce the simulated one.

The right-hand panels show the distribution of the difference between the fraction of stars measured and the fraction of stars expected: the distributions shown in the right-bottom panels may be approximated to Gaussian distributions centred on 0 and with a standard deviation $\lesssim 0.01$, confirming that the method adopted in Section 4 to measure the fraction of stars in each population is reliable.

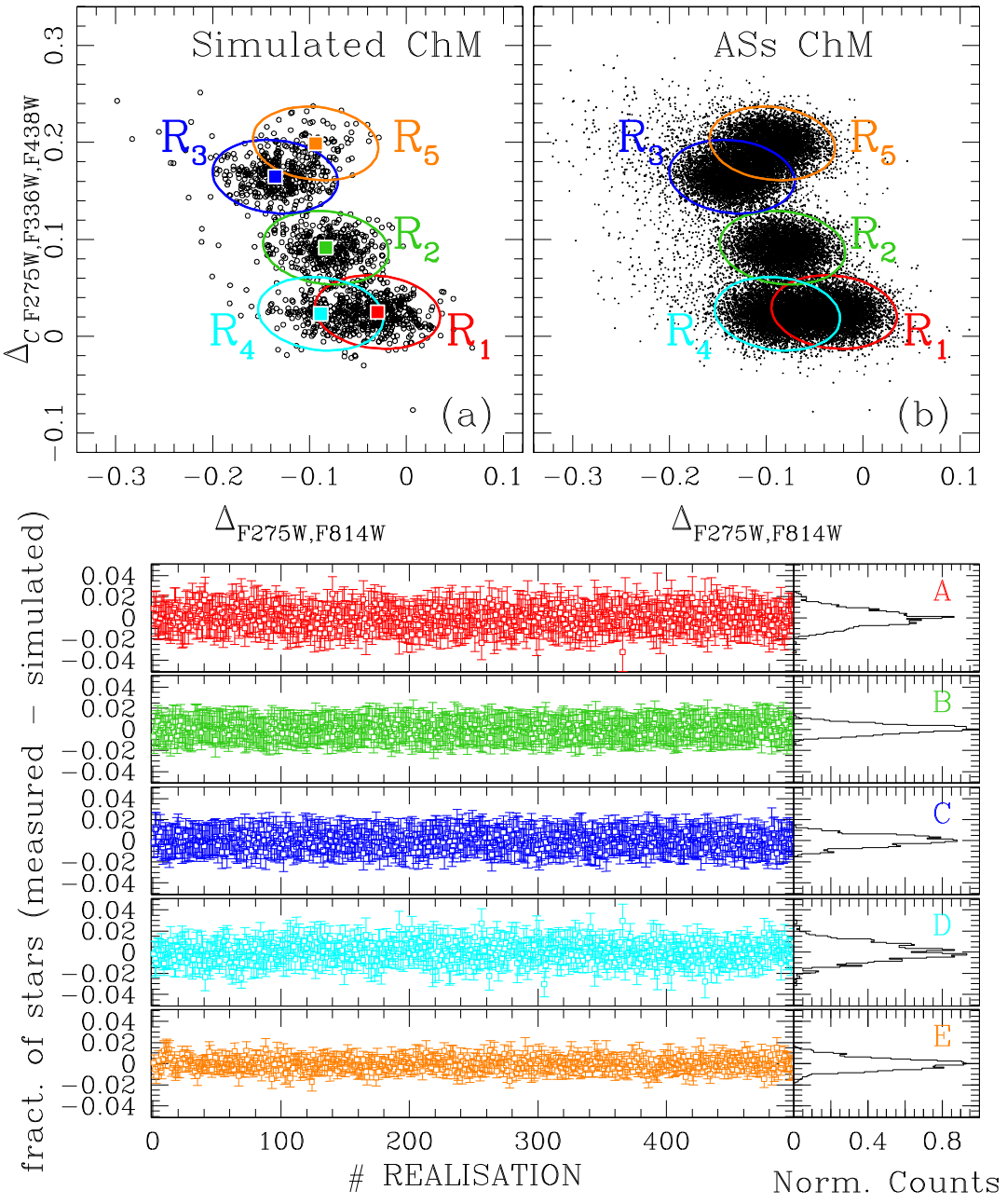

Figure A1. Panels (a) and (b) show the simulated and the ASs ChMs. The coloured eclipses are the regions R_i within which our analysis has been performed. Left-hand bottom panels show the difference between the measured and the expected fraction of stars at each of the 500 realizations of the simulated ChM. As shown in the right-hand bottom panels, the distributions of these differences are centred on zero.

This paper has been typeset from a TEX/LATEX file prepared by the author.